creative commons
COMMONS DEED

저작자표시-비영리-변경금지 2.0 대한민국

이용자는 아래의 조건을 따르는 경우에 한하여 자유롭게

- 이 저작물을 복제, 배포, 전송, 전시, 공연 및 방송할 수 있습니다.

다음과 같은 조건을 따라야 합니다:

저작자표시. 귀하는 원저작자를 표시하여야 합니다.

비영리. 귀하는 이 저작물을 영리 목적으로 이용할 수 없습니다.

변경금지. 귀하는 이 저작물을 개작, 변형 또는 가공할 수 없습니다.

- 귀하는, 이 저작물의 재이용이나 배포의 경우, 이 저작물에 적용된 이용허락조건을 명확하게 나타내어야 합니다.
- 저작권자로부터 별도의 허가를 받으면 이러한 조건들은 적용되지 않습니다.

저작권법에 따른 이용자의 권리는 위의 내용에 의하여 영향을 받지 않습니다.

이것은 이용허락규약(Legal Code)을 이해하기 쉽게 요약한 것입니다.

Disclaimer

dCollection

공학석사학위논문

Variable-Fidelity 방법을 통해 종방향 안정성과 저피탐성이 고려된 무인 전투기 플랜폼 최적화

Planform optimization of Unmanned Combat Aerial Vehicle considering longitudinal stability and Low-Observability using Variable-Fidelity Method

2020 년 2 월

서울대학교 대학원

기계항공공학부

양 선 웅

ABSTRACT

Considering the mission profile of the Unmanned Combat Aerial Vehicle(UCAV), efficient long-range and long-endurance flight must be available for penetrating enemy lines with weapons. At the same time, survivability undetected by enemy radar and moderate stability are needed. As a result, it is necessary to consider not only aerodynamics but also various performances from the design stage. In particular, due to the vortex generated from the leading edge, a high fidelity solver is required for the flow analysis. Existing studies, however, have an obvious limitation in that they considered only aerodynamic characteristics or used low fidelity flow solver though with consideration of other characteristics of UCAV.

Accordingly, optimization of the UCAV planform with RANS flow solver and Radar Cross Section(RCS) analysis is conducted in this research. A generic measure of aerodynamic performance, L/D at cruising flight and for considering the stability during the climbing, maximum available lift before pitchbreak onset where aircraft loses longitudinal stability are set to be objectives. Also, RCS is regarded as a constraint for Low-Observability of the UCAV. Accordingly, to reduce excessive computational cost due to the multi-point and multi-disciplinary design, Variable Fidelity Modeling(VFM) is used as a Hierarchical Kriging surrogate model. The Pareto set is derived from the Multi-Objective Genetic Algorithm in the constructed surrogate model, and three

configurations on the Pareto set were selected and analyzed through high fidelity analyses. As a result, the performance of the two objectives improves than the baseline, and the sensitivity analysis is conducted to analyze how their trends move as the design variables change. This study has significance in that it improves the performance of cruising flight and longitudinal stability of climbing flight while assuring Low-Observability of the UCAV planform.

Keywords : UCAV, Aerodynamic performance, Low-Observability, Pitchbreak, VFM, Hierarchical Kriging, Multi-Objective Genetic Algorithm

***Student Number*：2018-29313**

LIST

LIST OF FIGURES

LIST OF TABLES

I. Introduction

A. Introduction of Unmanned Combat Aerial Vehicle

UCAV(Unmanned Combat Aerial Vehicle) is a drone which operates on the battlefield. When compared to the existing manned fighters, the pilot's maneuvering equipment is unnecessary so that the weight and size can reduce, and also operable in extreme environments due to the unlimited endurance of the pilot[1]. Considering the mission profile of the UCAV, efficient long-range and long-endurance flight must be available for penetrating enemy lines with weapons. Simultaneously, survivability undetected by enemy radar during the infiltration and moderate stability are needed. Therefore, it is designed by adopting Blended Wing Body(BWB) in which the fuselage and the wing are connected smoothly. This configuration contributes to the low interference drag, radar cross section(RCS), and also the fuselage itself generates lifting force so that it has a higher L/D than conventional designs[2, 3, 4]. Among these BWB shapes, UCAV is divided into delta wing type(Figure 1) and double delta wing type(Figure 2). In delta wing configuration, fuselage and wing's leading-edge sweep angles are identical. On the other hand, double delta wing has a distinct sweep angles so that there exists the crank. An additional feature of UCAV configuration is its tailless planform, which is related to

the survivability. For Low-Observability(LO), the vehicle does not use tail to minimize RCS in that the tail wing increases the RCS due to discontinuity, but which plays an essential role in flight stability[5, 6]. Consequently, UCAV has unstable aerodynamic characteristics, and especially for the longitudinal stability, nonlinear variation of pitch-up moment occurs at a certain range of angle of attack(AoA)[7, 8]. This phenomenon is referred to as pitchbreak, and it is found out that this undesirable phenomenon is due to the separation over the wing tip region which causes the loss of lift behind the moment center causing the nose-up moment[9].

Thus, UCAV has aerodynamic characteristics that are disadvantageous in terms of stability compared to other fighters due to the planform design considering the LO characteristics. Nangia et al. showed that different planforms of UCAV can have distinct stability characteristics[10]. Also, Taha[11] indicated the degradation of aerodynamic performance when considering LO characteristics in the planform design. He performed X-47B configuration's structural and aerodynamic planform optimization without considering the LO characteristics, which concludes that it is superior with regard to drag and longitudinal stability compared to the baseline, which additionally considers LO characteristics. Therefore, these two characteristics need to be considered together from the conceptual design, which has to satisfy both the aerodynamic performance and the

survivability simultaneously due to the conflicting relationship between those[12]. In conclusion, UCAV's unique mission profile and planform make it necessary to take into account the aerodynamic performance for cruising flight, longitudinal stability, and Low-Observability all together from the planform design stage.

Figure 1 Boeing Phantom Ray(delta wing)

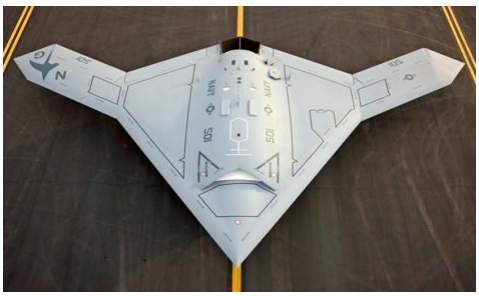

Figure 2 Northrop Grumman X-47B(double delta wing)

B. Research Objectives

In recent years, numerous researches on UCAV have been carried out under its need in future warfare. A number of the previous studies are about flow phenomenon analysis or detail design of pre-existed UCAV planform. For example, Schütte et al.[13] analyzed SACCON configuration through wind-tunnel experiments and Reynolds-Averaged Navier-Stokes(RANS) calculations to understand the overall flow physics. Also, Nangia et al.[14] investigated aerodynamic characteristics modifying only airfoil sections based on the MULDICON planform. Zenkner[15] and Aref et al.[16] each presented the design of the engine and S-duct intake for the MULDICON UCAV. For UCAV 1303 configuration, McParlin et al.[9] examined the effect of leading edge radius, Reynolds number and Mach number on aerodynamics, and Schütte et al.[17] additionally considered airfoils, twist angles and engine integration. For the investigation of the pitchbreak phenomenon, Shim[8] studied the effect of vortex generator(VG) on pitchbreak control, and Lee[18] optimized the VG array to maximize the pitch-up delay for the UCAV 1303 planform. Also, Atkinson[19] studied the effect of deployable Rao Vortex Flaps on the pitching moment.

There are also a number of researches on the UCAV planform design. Jeon[20] and Tyan[21] performed multidisciplinary optimization of UCAV planform by aerodynamic analysis, weight estimation, mission analysis and stability & control analysis. Jeon implemented aerodynamic analysis using Vortex Lattice Method(VLM), and Tyan used VLM as a low fidelity analysis and RANS as a high fidelity analysis. Pan[22] also optimized UCAV planform analyzing flow by panel method and structure by Finite Element Method(FEM). Furthermore, due to the trade-off relationship between aerodynamic and LO characteristics mentioned before, they are often examined together at the design process of UCAV. Tianyuan[23] calculated flow characteristics by potential flow, RCS by Physical Optics(PO) approximation method and allowable structural weight by FEM. Additionally, Jo[24] performed low fidelity flow analysis by panel method and high fidelity by Euler solver, Sepulveda[25] and Lee[26, 27] by single fidelity potential flow, all of which calculated RCS by PO method. These previous studies performed the optimization of the UCAV, but used a low fidelity flow solver for aerodynamic analysis. However, in the UCAV configuration, strong vortex develops along the leading edge from the apex at the high AoA region[28, 29, 30]. Since the formation of vortices has an enormous influence on the pitching moment, it is essential to use a high fidelity flow solver like RANS which can consider the viscous effect rather

than potential flow or Euler's non-viscosity analysis in the design process considering longitudinal stability[31, 32, 33].

UCAV planform optimization considering aerodynamic and RCS using RANS solver requires huge computational time due to the large design space and the use of high accuracy but expensive solver. Furthermore, multi-point flow analysis is conducted in this study : for cruising performance and longitudinal stability at climbing flight. Therefore, there are obvious limitations on the optimization using general methods. Especially for the climbing flight condition, calculations need to be performed as the AoA increases. Therefore, this problem with the computation is solved by variable fidelity model(VFM) in this research. Two levels of fidelity are used for CFD and RCS analysis, and these results are combined to construct the surrogate model and the optimization is progressed.

II. Methodology

A. Flow Analysis

i. Flow Solver

For flow analysis in this research, KFLOW solver is used[34, 35]. KFLOW is a RANS based Computational Fluid dynamics(CFD) solver where its governing equations are as below[36],

$$\frac{\partial Q}{\partial t}+\frac{\partial F}{\partial x}+\frac{\partial G}{\partial y}+\frac{\partial H}{\partial z}=\frac{\partial F_v}{\partial x}+\frac{\partial G_v}{\partial y}+\frac{\partial H_v}{\partial z} \tag{1}$$

$$\mathrm{Q}=\begin{pmatrix}\rho\\ \rho u\\ \rho v\\ \rho w\\ \rho e\end{pmatrix},$$

$$\mathrm{F}=\begin{pmatrix}\rho u\\ \rho u^2+p\\ \rho uv\\ \rho uw\\ u(\rho e+p)\end{pmatrix},\mathrm{G}=\begin{pmatrix}\rho v\\ \rho uv\\ \rho v^2+p\\ \rho vw\\ v(\rho e+p)\end{pmatrix},H=\begin{pmatrix}\rho w\\ \rho uw\\ \rho vw\\ \rho w^2+p\\ w(\rho e+p)\end{pmatrix} \tag{2}$$

$$\mathrm{e}=\frac{p}{\rho(\gamma-1)}+\frac{1}{2}(u^2+v^2+w^2) \tag{3}$$

$$F_v=\begin{pmatrix}0\\ \tau_{xx}\\ \tau_{yx}\\ \tau_{zx}\\ u\tau_{xx}+v\tau_{xy}+w\tau_{xz}-q_x\end{pmatrix},$$

$$G_v=\begin{pmatrix}0\\ \tau_{xy}\\ \tau_{yy}\\ \tau_{zy}\\ u\tau_{xy}+v\tau_{yy}+w\tau_{zy}-q_y\end{pmatrix},$$

$$H_v = \begin{pmatrix} 0 \\ \tau_{xz} \\ \tau_{yz} \\ \tau_{zz} \\ u\tau_{xz} + v\tau_{yz} + w\tau_{zz} - q_z \end{pmatrix} \tag{4}$$

$$\tau_{ij} = \mu\left(\frac{\partial u_i}{\partial x_j} + \frac{\partial u_j}{\partial x_i}\right) - \frac{2}{3}\mu\delta_{ij}\frac{\partial u_k}{\partial x_k} \tag{5}$$

where ρ means density, p means pressure, γ is specific heat ratio and $\mathrm{u, v, w}$ each means velocity of x, y, z direction. Also, Q means conservative variables, $\mathrm{F, G, H}$ mean inviscid flux vectors and F_v, G_v, H_v mean viscous flux vectors. This structured grid based solver has various options for turbulence models and numerical schemes.

Every CFD analysis used in this study adopts Menter's k-ω shear stress transport(SST) turbulence model[37]. This model is known to be good at prediction of flows with strong adverse pressure gradients and also separation due to its modification of eddy viscosity[38]. For the discretization method, Roe's Flux-Difference Splitting(Roe-FDS) with second order TVD Van Leer limiter is used for inviscid terms[39, 40] . For viscous terms, second order central difference is adopted. Also, backward Euler method with local time stepping is chosen and DADI method is used to approximate inverse matrix[41]. All analysis is conducted assuming steady-state and thanks to the symmetric planform of UCAV geometric model, only half body is used for the calculation and symmetric boundary condition is applied for time efficiency.

ii. Flow Solver Validation

For validation of KFLOW solver, SACCON UCAV is used for the calculation. To compare calculated pressure distribution with experimental data[13], adopted flow settings are summarized in Table 1. Especially, for validation in situation where the influence of vortex is predominant, high AoA(15.3˚) is selected. Total 9.5 million volume cells are generated as Figure 3. Overall planform and certain sections of SACCON used for comparing pressure distribution are visualized in Figure 4. As a result, Figure 5 and 6 show experimental data and RANS solver's calculated data. Additionally, Euler solver's data are shown to prove that Euler solver is inaccurate to predict vortex flow. RANS solver using k-ω SST turbulence model calculates pressure distribution similar to the experiment, whereas Euler solver predicts wrong vortex compared to the RANS solver. To summarize, KFLOW RANS solver and its settings are adequate for calculating flow field around UCAV configuration at high AoA region where leading-edge vortex is observed. Also, from Euler solver's discrepancy with the experiment, the necessity of RANS solver is emphasized despite its high computational cost.

Table 1 Flow condition for validation

Flow parameters	Value
Mach number	0.15
Reynolds number	1.6×10^6
AoA	15.3°

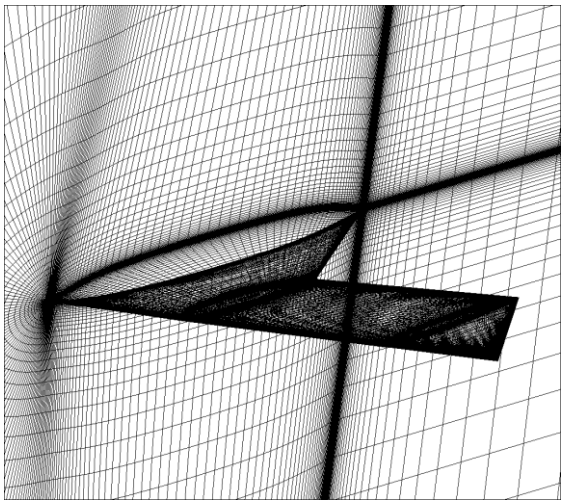

Figure 3 Grid system used in validation

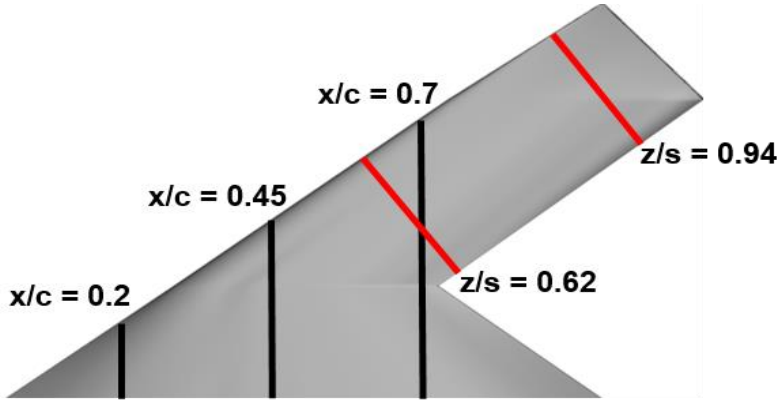

Figure 4 Slice locations used to compare pressure distribution

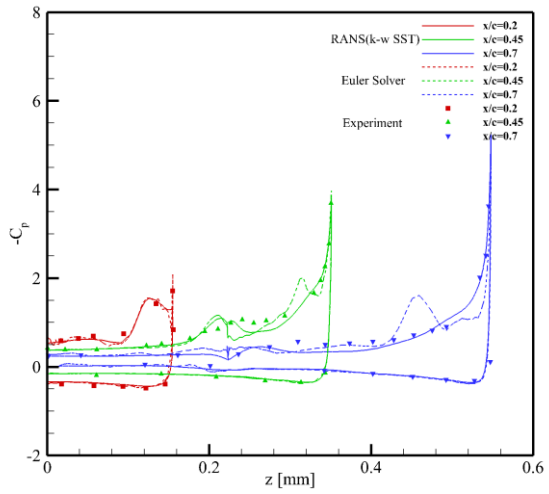

Figure 5 Pressure distribution comparison of x slices

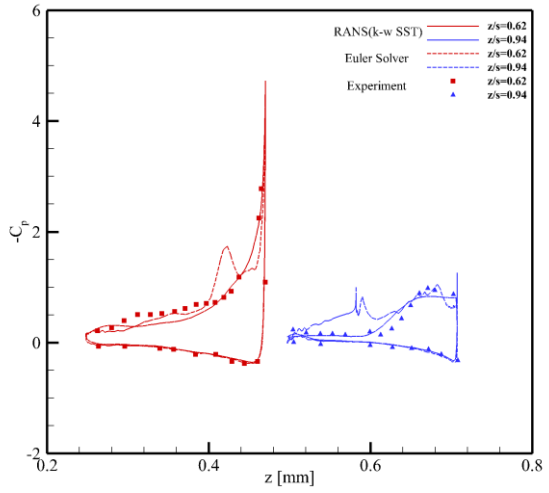

Figure 6 Pressure distribution comparison of z slices

B. RCS Analysis

i. Definition of RCS

Radar Cross Section(RCS) is a well-known criterion for measuring observability of an object from the radar. Its definition is as Eq. (6),

$$\sigma = \lim_{R\to\infty} 4\pi R^2 \frac{\left|\vec{E}_s\right|^2}{\left|\vec{E}_i\right|^2} \tag{6}$$

where R is a distance and $\vec{E}_s$, $\vec{E}_i$ each means scattered and incident electric field intensities from the target[42]. RCS of an object is the cross-sectional area of a perfectly reflecting sphere which produces the same strength reflection as the object. For example, if an object has a RCS of $1m^2$, it implies that its strength of reflection is equal to a sphere with a cross-section area of $1m^2$. It can be influenced by polarization and frequency of the incident wave and target object's properties(including angle with respect to the incident wave, electrical size and material). Its unit is originally m^2, but decibels relative to a square meter(dBsm) is used commonly as Eq. (7).

$$\sigma[\text{dBsm}] = 10\log(\sigma[m^2]) \tag{7}$$

At X-band frequency, RCS of a bird is known to be -20 dBsm and for the insect, -30dBsm. To calculate RCS, analysis using computational electromagnetic(CEM) is needed and its methods can be divided into two types as Figure 7[43]. One is a full-wave method, which is based on the integral or differential Maxwell equations. Examples of full-wave methods are Finite Difference Time Domain(FDTD), Method of Moments(MoM) and Finite Element Method(FEM). The other is an asymptotic method. It has basis on approximations of Maxwell equations and due to its underlying approximations(high frequency situation), great accuracy can be achieved in high frequency analysis[44]. Its examples are Physical Optics(PO), Geometrical Optics(GO) and Shooting and Bouncing Rays(SBR). In this research, computation of RCS is conducted for the measure of UCAV's observability.

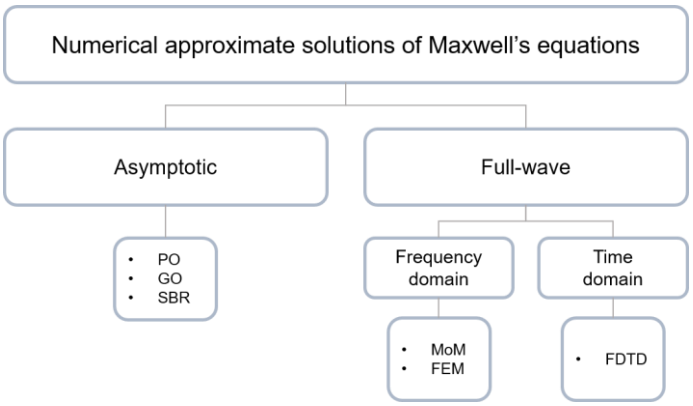

Figure 7 Methods of CEM

ii. RCS Solver

For RCS analysis, ANSYS HFSS v193 is used. It offers various solvers like FEM, MoM and SBR. However, full-wave methods need excessively high computational time for high frequency analysis. In that sense, SBR solver is adopted in this study. SBR method can consider multiple bounce effects and shadowing effects. It includes other asymptotic methods and its process is summarized at Figure 8[45]. In HFSS, SBR with advanced diffraction and creeping wave physics for increased accuracy is available[46]. In this study, SBR solver is used with Physical Theory of Diffraction(PTD) and Uniform Theory of Diffraction(UTD). Also, creeping wave physics for scattering in shadowed regions and maximum 3 bounces are considered. For reason to be mentioned later, directions of incident wave(10 GHz horizontally polarized plane wave) are limited to 0˚~90˚ azimuth angle.

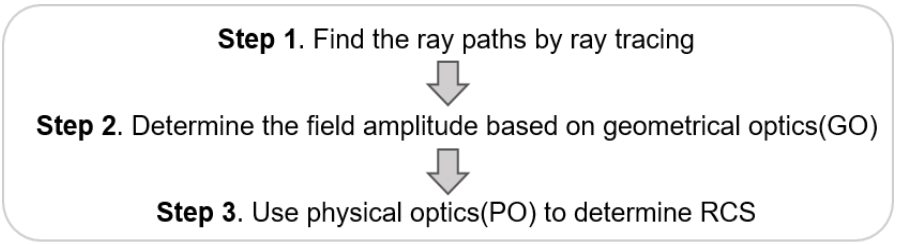

Figure 8 Process of SBR method

iii. RCS Solver Validation

Validation of the solver used for RCS analysis is carried out with double ogive model which is a benchmark case of NASA. Figure 9 visualizes the used model and directions of incident wave. Exact geometric information of the model can be found in reference [47]. Because RCS analysis of the UCAV is conducted at X band frequency, validation also uses 9 GHz horizontally polarized plane wave. For directions of the incident wave, azimuth angle is analyzed at 1˚ intervals from 0˚ to 180˚ and surface of the model is assumed as perfect conductor(PEC). Finally, experimental data are compared with calculated RCS by SBR solver as Figure 10. Where azimuth angle is 60˚~120˚, SBR solver's prediction suits well with the measurement. However, in the region of 0˚~60˚ and 120˚~180˚, SBR data show large discrepancy with the experiment. In this azimuth range, due to the sharp edges of the model at 0˚ and 180˚, diffraction effects can be dominant. In that sense, employed SBR solver, which is an asymptotic CEM method seems to have difficulties at handling sharp edge scattering mechanisms despite PTD and UTD theory. Also, considering asymptotic methods have an advantage at accuracy for electrically large object($\text{object length} > 10 * \text{wavelength}$) analysis, scale of the double ogive model(25.4 cm) can be somewhat small compared to the wavelength

of the incident wave(3.3 cm). For this reason, RCS analysis of UCAV configuration is restricted to 0˚~90˚ azimuth angle region to evade the influence of sharp trailing edges.

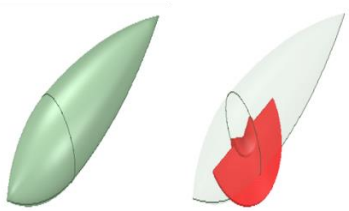

Figure 9 Double ogive model(left) and directions of incident wave(right)

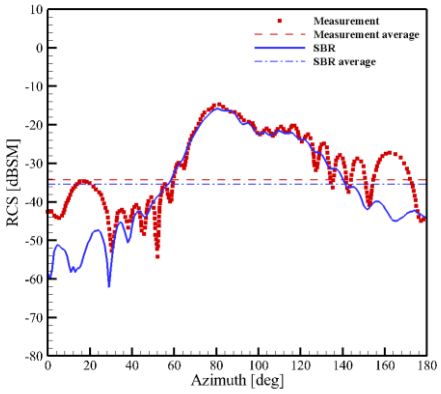

Figure 10 Double ogive's RCS comparison with experiment and SBR

C. Optimization Methods

i. Hierarchical Kriging

Due to the expensive computational cost of direct optimization, surrogate model is used in this study(Figure 11). Optimization using surrogate model is efficient because of its basis on the interpolation or approximation[48]. Among various surrogate models, kriging is popular for its prominent performance in multidimensional and highly nonlinear situations[49, 50]. To construct the surrogate model, Design of Experiments(DoE) needs to be performed for selecting sampling points used in interpolation. In this study, Latin Hypercube Sampling(LHS) method is used for DoE. After DoE, as a surrogate model, hierarchical kriging is selected[51, 52]. It is an extension of kriging model for VFM problems. To predict high fidelity model, data from lower fidelity are used as a model trend. In that sense, although lower fidelity data may

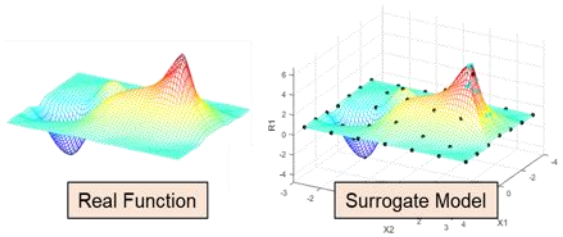

Figure 11 Schematic description of the surrogate model

have a large discrepancy from high fidelity data, its trend should conform well with the high fidelity data's trend(Figure 12). For two levels fidelity case, conventional kriging model is constructed based on the low fidelity data as Eq. (8) where $\beta_{0,lf} = (1^T R_{lf}^{-1} 1)^{-1} 1^T R_{lf}^{-1} y_{S,lf}$, r_{lf} is the correlation vector between the unproved point and the calculated points and $y_{S,lf}$ is sampling points of low fidelity model[53, 54].

$$\hat{y}_{lf}(x) = \beta_{0,lf} + r_{lf}^T(x) R_{lf}^{-1}(y_{S,lf} - \beta_{0,lf} 1) \tag{8}$$

After weight coefficients vector w is found by Eq. (9) which subjects to Eq. (10), final kriging model with high fidelity data is as Eq. (11)

$$\mathrm{MSE}[\hat{y}(\mathrm{x})] = \mathrm{E}[(w^T Y_S - \mathrm{Y}(\mathrm{x}))^2] \tag{9}$$

$$E\left[\sum_{i=1}^{n} w^{(i)} Y\left(x^{(i)}\right)\right] = E[Y(x)] \tag{10}$$

$$\hat{y}(x) = \beta_0 \hat{y}_{lf}(x) + r^T(x) R^{-1}(y_S - \beta_0 F) \tag{11}$$

where y_S is high fidelity data, Y_S is corresponding random quantities, $Y(x)$ is $\beta_0 \hat{y}_{lf}(x) + Z(x)$, $Z(x)$ is stationary random process, β_0 is constant factor and F is the estimation from low fidelity kriging model. These steps can be repeated for

multilevel fidelity case as Figure 13 and note that the final kriging model uses low fidelity kriging function $\hat{y}_{lf}(x)$ as a global trend. For this reason, it is necessary to verify selected low fidelity data have similar trend with high fidelity data. If low fidelity model does not comply well with high fidelity model which is a desired function, hierarchical kriging surrogate model will be useless or even detrimental to the optimization. Accordingly, at the next part, grid convergence test will include trend comparison between low and high fidelity data.

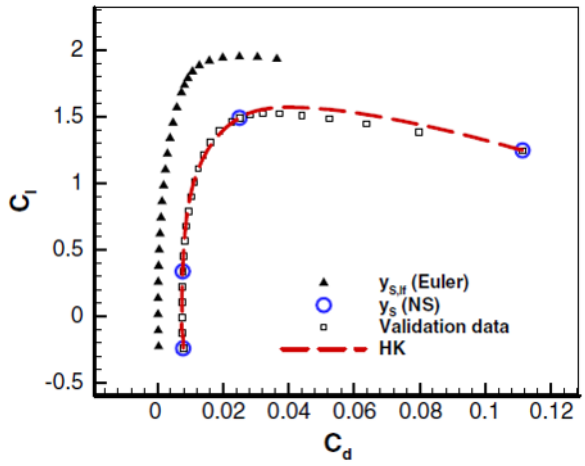

Figure 12 Example result of the hierarchical kriging[50]

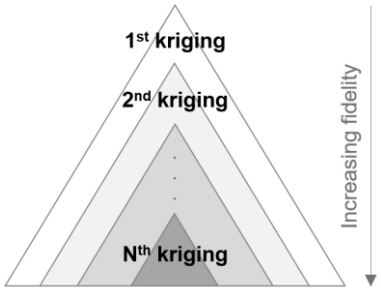

Figure 13 Schematic description of the hierarchical kriging

ii. Multi-Objective Genetic Algorithm

After the construction of surrogate model, the optimization method needs to be selected to find an global optimal solution. There are numerous methods for optimization : Simulated Annealing(SA), Particle Swarm Optimization(PSO), Game Theory Optimization(GT), Evolutionary Algorithm(EA), Genetic Algorithm(GA). Among these, GA has strength in discontinuity and multimodality problems due to its characteristics that do not need derivative information[55]. Additionally, it searches optimal solutions from a population of points, so that GA can be efficient in multi-objective problems and its process is depicted in Figure 14. First of all, GA initializes a

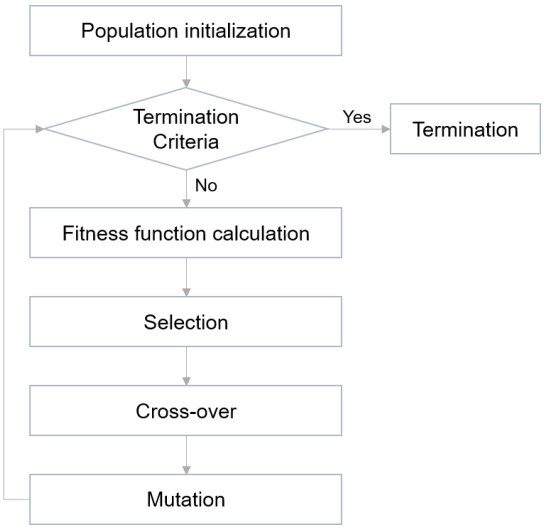

Figure 14 Schematic description of GA

population and calculates the fitness function of each. Then, it selects a couple of parents and applies cross-over and mutation procedure. Resultant new population replaces the past generation and these processes are repeated until the termination criterion is satisfied. For multi-objective problems in this study, Multi-Object Genetic Algorithm(MOGA) is used, so there can be no single optimal solution[56]. For representing optimal solutions, pareto optimal set is used to handle several optimal points as Figure 15[57].

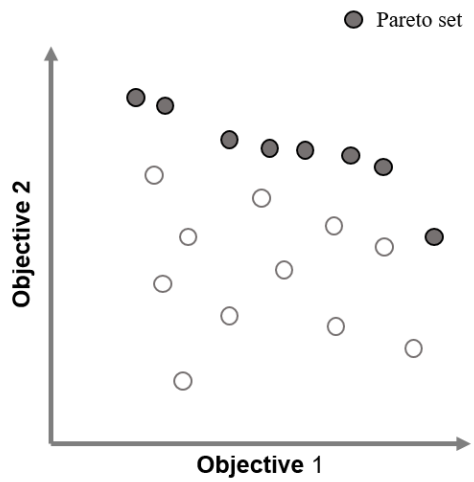

Figure 15 Pareto set in the problem of maximizing two objectives

D. Grid Convergence Test

As discussed earlier, it is crucial to verify low fidelity data have similar trend with high fidelity data before using hierarchical kriging surrogate model. For this reason, this part will discuss: 1) whether accuracy of high fidelity model is enough, 2) whether low fidelity model complies well with selected high fidelity model. In this research, VFM is conducted in CFD and RCS analysis with two level fidelities. Both analyses distinguish each fidelity by grid density used in calculation. Baseline configuration used in analyses is X-47B UCAV.

i. CFD Grid Convergence

Used information about flight condition for grid convergence of CFD analysis is as Table 2. Total 8 structured volumes grids are tested and their information is in Table 3.

Table 2 Flow conditions for CFD grid convergence test

Flow parameters	Value
Mach number	0.15
Reynolds number	9.12×10^6
AoA	0°
Altitude	At sea level

Table 3 Grids information for CFD grid convergence test

Grid type	Grid number	CPU time [hour]
1	2,000,000	19.2
2	3,200,000	31.2
3	3,600,000	36
4	4,800,000	48
5	7,000,000	67.2
6	9,400,000	91.2
7	12,600,000	127.2
8	16,400,000	165.6

After CFD analysis, calculated lift coefficients and drag coefficients are plotted on Figure 16. To inspect longitudinal stability for pitchbreak phenomenon, convergence of the pitching moment coefficients is also examined. Figure 17 shows that all of tested

grids have almost same values. Considering computational time and convergence of aerodynamic coefficients, grid type 3 is selected as low fidelity grid and grid type 6 as high fidelity grid. Then, trend of the selected grids are compared by L/D as AoA

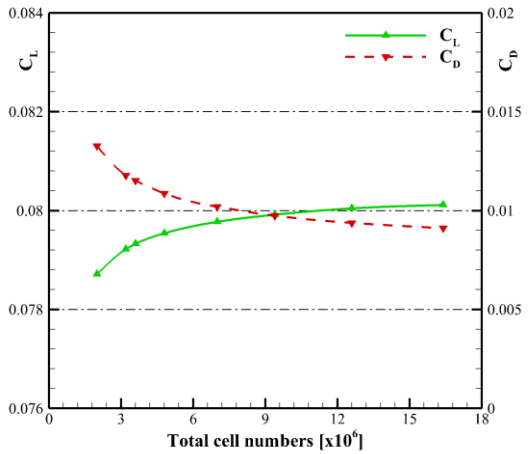

Figure 16 Lift and drag coefficients of tested grids

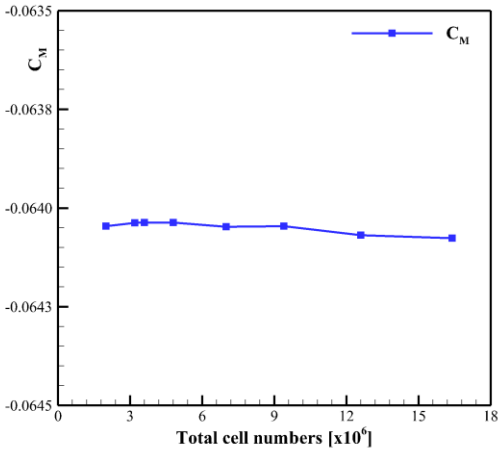

Figure 17 Pitching moment coefficients of tested grids

increases. Figure 18 compares grid type 3, 6 and 8. Grid type 8 is added because it is the most dense grid used in the grid convergence test. Overall tendency of low fidelity and high fidelity grids at the range of AoA 0˚ to 14˚ complies well with the finest grid(type 8). Moreover, both selected grids calculate maximum L/D at AoA 4˚ as the finest grid which implies optimal point of hierarchical kriging model using grid type 3 and 6 will be located near the optimal point of kriging model constructed only by grid type 8 while reducing computational cost. As a result, it is concluded that the selected low fidelity and high fidelity grids are suitable to build the hierarchical kriging model.

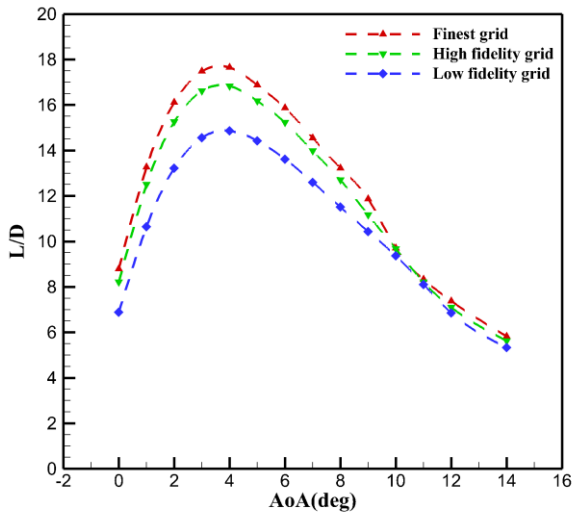

Figure 18 L/D trend of 3 grids

ii. RCS Grid Convergence

Table 4 summarizes RCS analysis conditions. Total 9 triangular surface grids are used for the grid convergence test and information about tested grids are on the Table 5. Averaged RCSs computed from these grids are shown in Figure 19. Unlike CFD, RCS analysis uses unstructured grids so that asymptotic convergence cannot be easily

Table 4 Analysis conditions for RCS grid convergence test

Analysis conditions	Details
Frequency	10 Ghz
Polarization	Horizontal
Material	PEC
Azimuth angle	0°~90°(0.5° intervals)
Elevation angle	0°
Radar type	Monostatic

Table 5 Grids information for RCS grid convergence test

Grid type	Grid number	CPU time [hour]
1	1,386	5.8
2	3,438	6.2
3	20,966	7
4	42,414	9.2
5	172,680	13.8
6	250,160	16.5
7	546,970	32.7
8	799,112	46
9	1,159,778	92.2

obtained. Nevertheless, oscillation around -27 dBsm is observed with grid type 3~9. From the computational time and values of average RCS of tested 9 grids, grid type 2 is chosen as low fidelity grid and grid type 7 as high fidelity grid. By inspecting model trend in Figure 20, it can be concluded that 3 grids(low fidelity grid, high fidelity grid and the finest grid) have similar trend of RCS with respect to the azimuth angle. All of

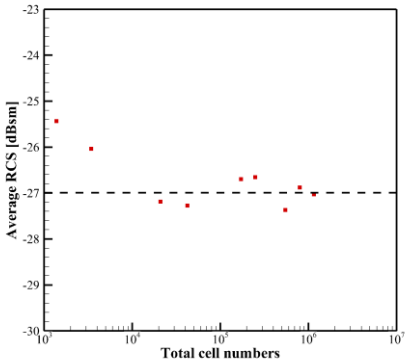

Figure 19 Average RCS of tested grids

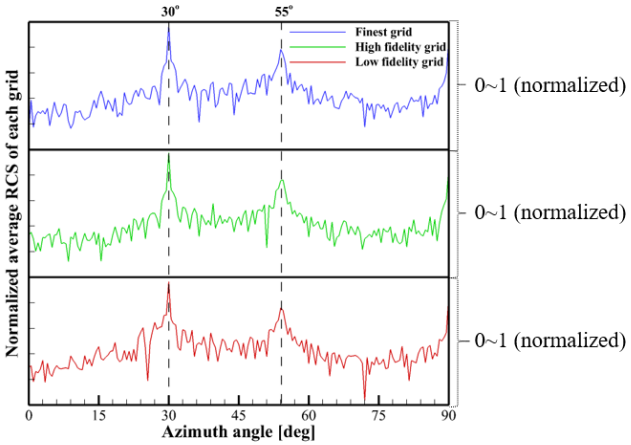

Figure 20 RCS trend of 3 grids

these grids estimate local maximum RCSs at azimuth angle 30˚ and 55˚. These angles are two sweep angles of the baseline model and naturally, local maximum RCSs are predicted there. In conclusion, it is verified that selected low fidelity and high fidelity grids are suitable for hierarchical kriging in RCS analysis.

III. Results and Discussions

A. Optimization Problem

i. Problem Definition

For optimization, baseline configuration is a real scale of X-47B UCAV same as the grid convergence test(Figure 21). From the baseline planform, total 10 design variables are adopted. Among them, 8 are general planform variables and other 2 variables are leading edge radius of the wing and wing tip angle. Leading edge radius is added because previous researches proved that it has a significant influence both on aerodynamic and RCS characteristics[32, 58]. Also, it is known that considering wing tip angle(Figure 22) can improve structural stiffness, wing loading, stability margin and reduce the drag[59].

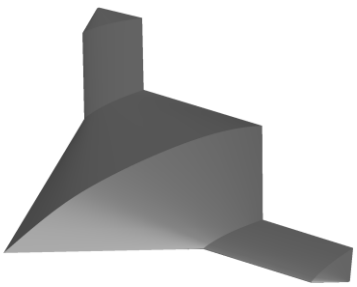

Figure 21 X-47B baseline configuration

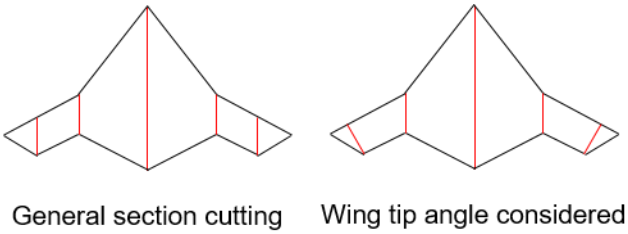

Figure 22 Wing tip angle consideration

As a result, selected 10 design variables are represented in Figure 23 and the design space is summarized in Table 6. Other planform variables are determined by chosen design variables based on the line alignment[60, 61]. Also, symmetric plane of the baseline UCAV is fixed for preventing drastic change of fuselage which can reduce the space for engine.

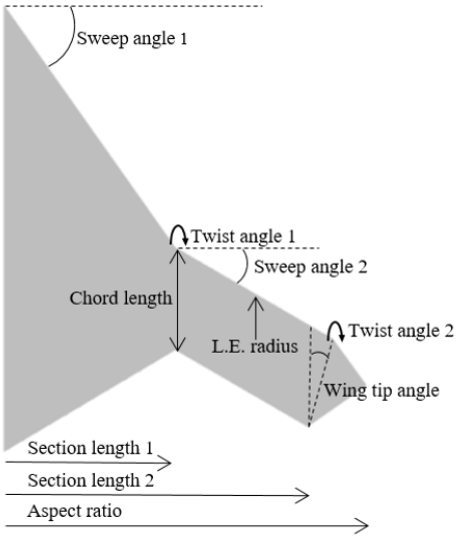

Figure 23 Design variables

Table 6 Design space

Design Variable	Design space			Design Variable	Design space		
	Lower	Base	Upper		Lower	Base	Upper
Sweep angle 1 [degree]	46.7	55	60.5	L.E. radius [mm]	0.0038	0.0051	0.0064
Sweep angle 2 [degree]	27	30	33	Chord length [mm]	2411.3	2679.2	2947.1
Twist angle 1 [degree]	-5	0	5	Section length 1 [mm]	4041	4490	4939
Twist angle 1 [degree]	-5	0	5	Section length 2 [mm]	7552	7950	8189
Wing tip angle [degree]	14.7	16.3	17.9	Aspect ratio	1.58	1.63	1.71

DoE in design space is implemented by LHS for each fidelity. For low fidelity model, 100 points are selected and 48 points for the high fidelity. Even distribution of 100 points of two twist angles in low fidelity model is depicted in Figure 24. After DoE process, construction of the hierarchical kriging surrogate model is progressed based on CFD and

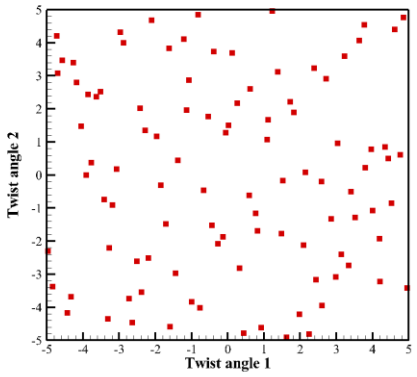

Figure 24 Points distribution of two twist angles for low fidelity model

RCS analysis data and by GA with 1024 populations and 100 generations, optimum pareto set is obtained. Then, 2 points selected by specific criteria from pareto sets are calculated by high fidelity analysis. If average error between estimation and calculation is more than 1.5%, these calculated 2 points are added as high fidelity sampling points and constructs hierarchical kriging again. These process is repeated until average error between estimation and calculation is below 1.5%. Overall process is depicted in Figure 25.

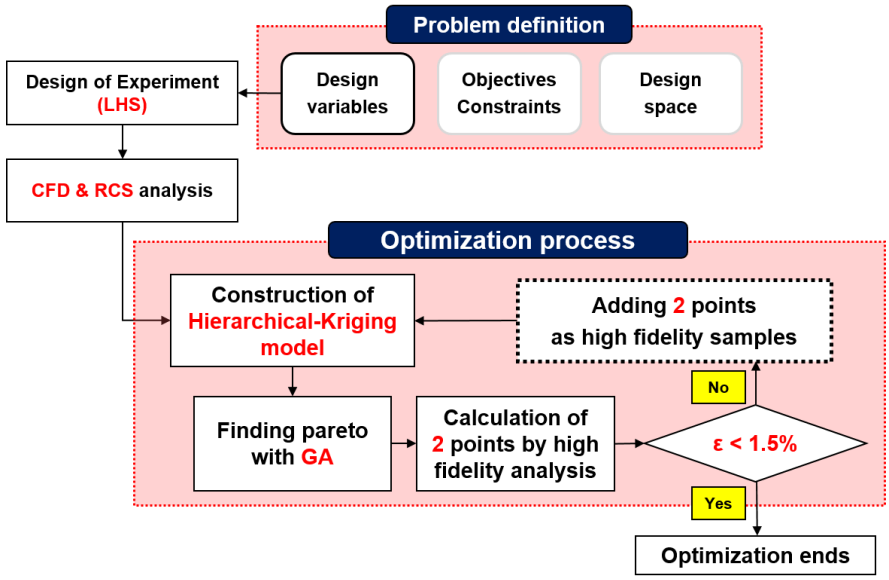

Figure 25 Flowchart of optimization process

Before optimization, objectives and constraints need to be set. Problem definition of this study is summarized in Table 7. Objective 1 is the L/D at cruising flight. This objective is the fundamental performance criterion for long endurance and long range flight. The other objective is to maximize the maximum available lift before the pitchbreak onset. This objective is calculated under climbing flight condition because pitchbreak phenomenon is important in climbing flight where high lift is required. Constraint 1 is to reduce weight of UCAV and constraint 2 is to obtain enough internal volume for storage space of equipment and fuel tank. Constraint 3 is for LO characteristics of UCAV planform. This is to prevent a degrade in stealthy performance while improving aerodynamic performance by 2 objectives. Parameters used in optimization from CFD and RCS analysis are explained in the next part: Methods of handling data.

Table 7 Problem definition

Objectives	1.	Maximize **cruising L/D**
	2.	Maximize maximum available $\mathbf{C_L}$ before **pitchbreak** at **climbing** flight
Constraints	1.	**Weight** < Baseline weight
	2.	**Volume** > Baseline volume
	3.	Average **RCS** < Baseline average RCS

ii. Methods of Handling Data

Flight conditions used for obtaining CFD data in optimization is summarized in Table 8. At cruising condition, UCAV should generate lift for its own weight which means trim condition needs to be analyzed. In this research, cruising condition is estimated with second order polynomial drag polar as Eq. (12)[62].

$$C_D = C_D^* + k(C_L^* - C_L)^2 \quad (12)$$

Using lift and drag coefficients from 3 cases with different AoA, drag polar over the whole AoA range can be predicted. Then, required lift coefficient for sustaining newly designed airframe is obtained by weight estimation of the planform and L/D at cruising flight is calculated by created drag polar. Before optimization, validation of prediction model of the drag polar is conducted. Figure 26 shows predicted drag polar with 3 cases(AoA 0˚, 3˚, 6˚) suits well with the calculated lift and drag of AoA 1˚, 2˚, 4˚, 5˚.

Table 8 Analysis conditions of CFD

Flight condition	Re[*10^6]	Mach	AoA[˚]	Altitude
Cruising	16.1	0.55	0, 3, 6	11km
Climbing	9.12	0.15	0~12 (2˚ interval)	At sea level

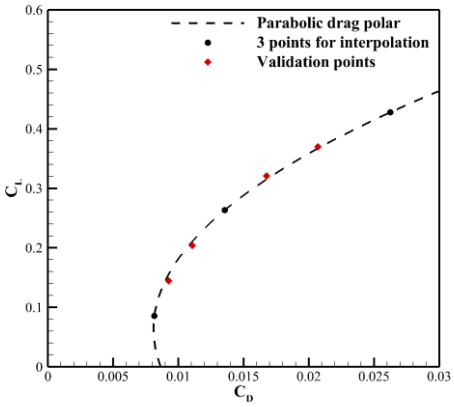

Figure 26 Validation of interpolated drag polar

Meanwhile, for the climbing flight, total 7 cases with varying AoA are analyzed. To investigate the pitchbreak phenomenon, range from 0˚ to 12˚ of AoA with 2˚ interval are calculated. Aerodynamic coefficients Cl, Cm are interpolated by 5th order polynomials with respect to AoA and its example of interpolating Cm is depicted in Figure 27. After the interpolation, criterion of pitchbreak needs to be defined. Static Stability Margin(SM) is used as a measure of pitchbreak onset. SM is defined as a distance in percent MAC from the neutral point($\bar{X}_{np}$) to the center of gravity($\bar{X}_{cg}$) and it can be also expressed as Eq. (13)[62].

$$\frac{dC_M}{d\alpha} = -\frac{dC_L}{d\alpha} * \left(\bar{X}_{np} - \bar{X}_{cg}\right) = -\frac{dC_L}{d\alpha} * \text{SM} \tag{13}$$

Longitudinal stability of the aircraft is considered as stable when SM is positive and unstable when negative. By the interpolation of Cl and Cm, one can get $\frac{dC_M}{d\alpha}$ and $\frac{dC_L}{d\alpha}$ at any AoA so that SM can be calculated. In this study, it is assumed that SM above -10% is regarded as stable by the operation of control surfaces. It is determined as a pitchbreak onset when SM starts to fall below -10%. In that sense, maximum available lift before pitchbreak can be obtained and it is used as an objective 2.

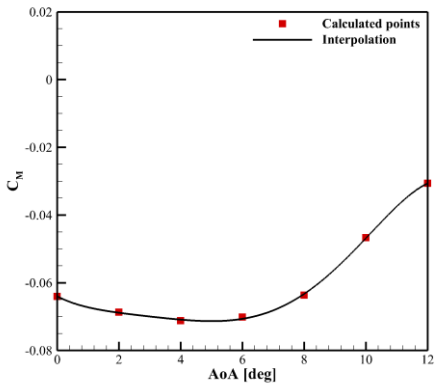

Figure 27 Interpolation of pitching moment coefficients

For the optimization constraints, the weight of the designed planform is assumed to be proportional to projected area of the baseline. For example, if a new design has a 10% larger projected area than the baseline, its weight is predicted to be 10% heavier. The weight of the baseline configuration is assumed to be 6350kg, which is the empty weight of the X-47B UCAV. Volume of the planform is calculated by CAD program which generates geometries of various UCAV planforms. Lastly, constraint 3 is an averaged RCS of various azimuth angles. Overall process of data transfer is depicted in Figure 28.

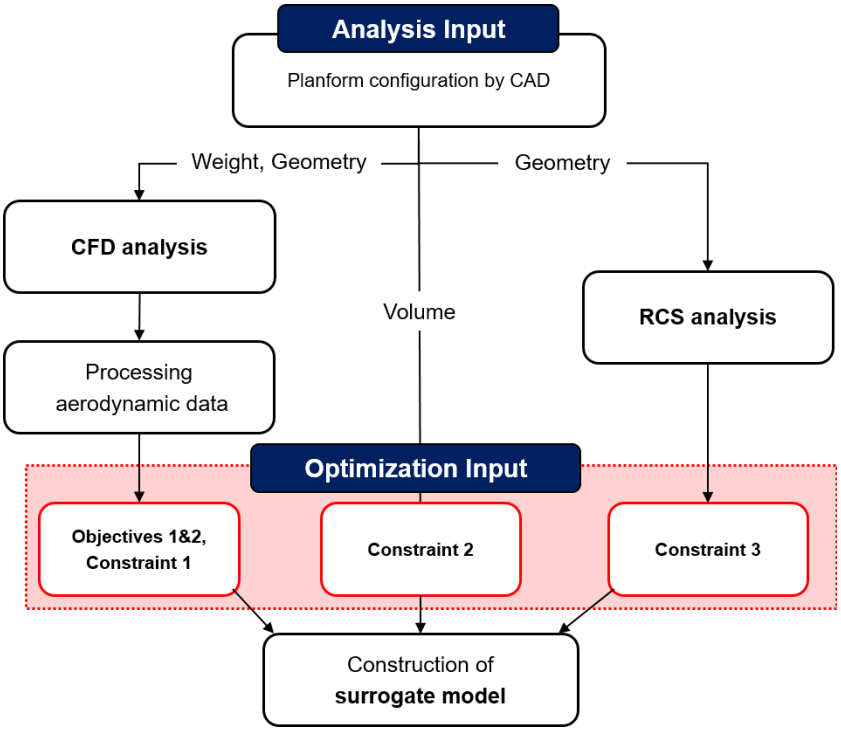

Figure 28 Overall process of data transfer

B. Results

For error criterion ε<1.5%, 18 high fidelity points are added as adaptive sampling before optimization ends and final sampling points used for the hierarchical kriging are 100 for low fidelity and 66 for high fidelity. Total computational time for the optimization is summarized in Table 9. For ensuring reliability of the constructed hierarchical kriging surrogate model, cross-validation is conducted and its results are depicted in Figure 29. Distribution of calculated and estimated values indicate that constructed surrogate model fits well with the calculated data. Also, most of the standardized residuals are in the range -3 to 3, which means they are within the 99.7% confidence interval. Then, pareto set is obtained and compared with the baseline in Figure 30 based on the verified surrogate model. From the pareto set, 3 points(named OPT1, 2, 3) are selected and calculated by the high fidelity analysis. Design variables and planform comparison with the baseline is shown in Table 10 and Figure 31.

Table 9 Computational time for the optimization

Analysis	Fidelity	CPU time [day]	Total CPU time [day]
CFD analysis	Low	110	422
	High	312	
RCS analysis	Low	1.6	7.6
	High	6	
Total			429.6

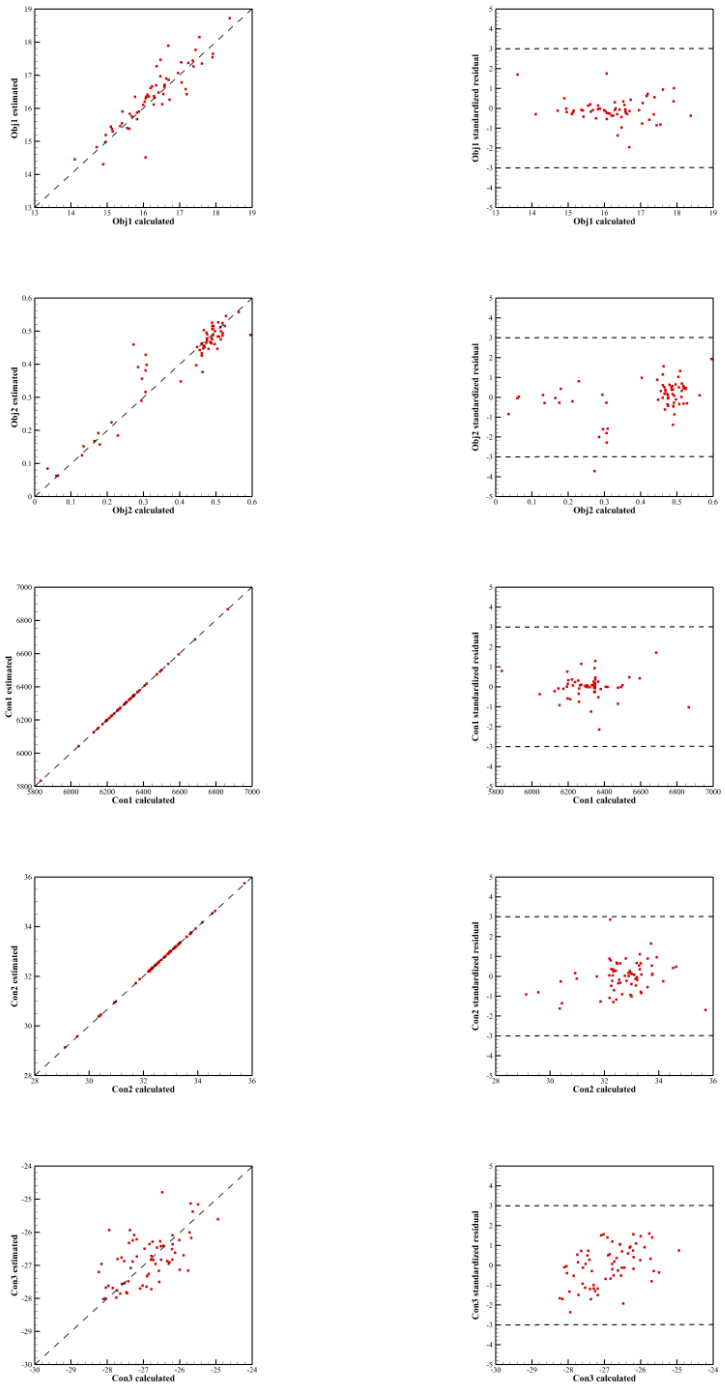

Figure 29 Cross-validation of the final surrogate model

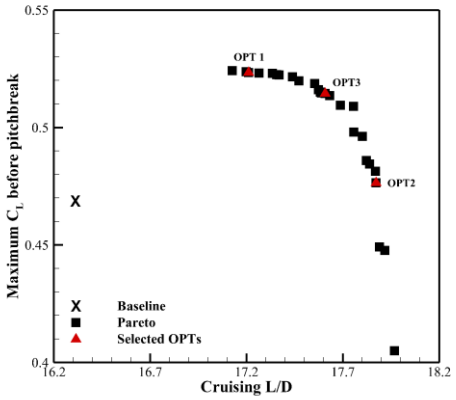

Figure 30 Pareto set

Table 10 Design variables of selected optimums

	Baseline	OPT1	OPT2	OPT3
Sweep angle 1 [degree]	55	54.60914 (-0.71%)	53.78723 (-2.21%)	54.22668 (-1.41%)
Sweep angle 2 [degree]	30	32.98614 (+9.95%)	32.95469 (+9.85%)	32.99101 (+9.97%)
Twist angle 1 [degree]	0	1.945702 (-)	2.072616 (-)	1.988399 (-)
Twist angle 2 [degree]	0	0.1033177 (-)	0.07836269 (-)	-0.1135503 (-)
Wing tip angle [degree]	16.3	17.80891 (+9.26%)	17.73968 (+8.83%)	17.78316 (+9.10%)
L.E. radius [mm]	0.0051	0.004009981 (-21.06%)	0.003881432 (-23.59%)	0.003973279 (-21.79%)
Chord length [mm]	2679.2	2497.678 (-6.77%)	2498.572 (-6.74%)	2495.831 (-6.84%)
Section length 1 [mm]	4490	4776.273 (+6.37%)	4776.091 (+6.37%)	4783.344 (+6.53%)
Section length 2 [mm]	7950	7594.138 (-4.48%)	7560.62 (-4.90%)	7583.941 (-4.61%)
Aspect ratio	1.63	1.651468 (+1.59%)	1.650819 (+1.55%)	1.651313 (+1.58%)

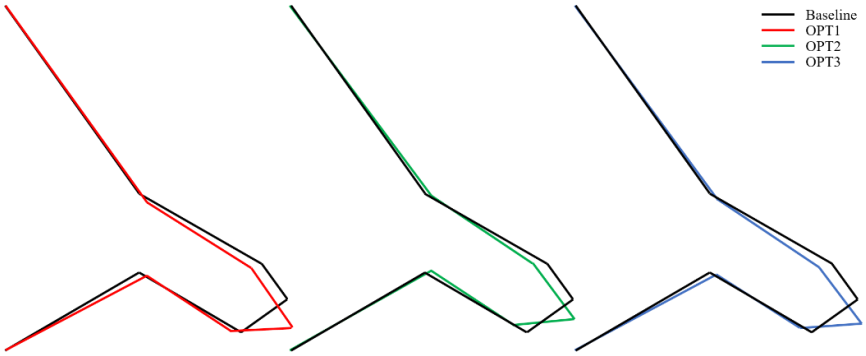

Figure 31 Planform comparison of selected optimums with the baseline

Calculated objectives and constraints of selected points on the pareto are compared with the baseline in Table 11. OPT1 and OPT3 have better performance than the baseline with respect to both objectives: obj1 increases 2.76% and obj2 increases 3.13% for OPT1, obj1 increases 3.21% and obj2 increases 1.85% for OPT3. They have moderate performance for both objectives compared to the baseline. However, OPT2 has superior cruising L/D(+8.04%) but shows inferior performance with maximum available lift

Table 11 Optimization results

	Baseline	**OPT1**	**OPT2**	**OPT3**
L/D @ cruising	16.31158	16.76195 (+2.76%)	17.62246 (+8.04%)	16.83575 (+3.21%)
Max C_L before pitchbreak	0.4686	0.483259 (+3.13%)	0.461719 (-1.47%)	0.477275 (+1.85%)
Weight	6350	6347.05 (-0.05%)	6339.231 (-0.17%)	6347.051 (-0.05%)
Volume	32.1733	33.2476 (+3.34%)	33.2415 (+3.32%)	33.2821 (+3.45%)
Average RCS	-27.3702	-28.1721 (-2.93%)	-28.4358 (-3.89%)	-28.6759 (-1.12%)

before pitchbreak(-1.47%). All of the selected optimums satisfy constraints and in terms of average RCS, OPT2 shows the best performance. For the further investigation, L/D at cruising flight condition of 3 calculated cases are plotted in Figure 32(left). Except at AoA 6˚, they have higher L/D than baseline. One important thing in this figure is that OPT2 has lower L/D at 6˚ than other optimums but similar L/D at 0˚ and 3˚. This fact indicates that due to the interpolation of the drag polar with second order polynomial, L/D at low AoA can be predicted excessively higher than others due to the aerodynamic coefficients at AoA 6˚. Considering cruising flight that generates the lift of its own weight is around AoA 1˚ in this study, OPTs have superior L/D for the cruising flight condition which can be induced by the L/D at AoA 0˚ and 3˚(especially 0˚), but method of predicting drag polar needs to be refined for more precise analysis. For the climbing flight condition, OPTs have almost similar L/D values with respect to AoA as shown in

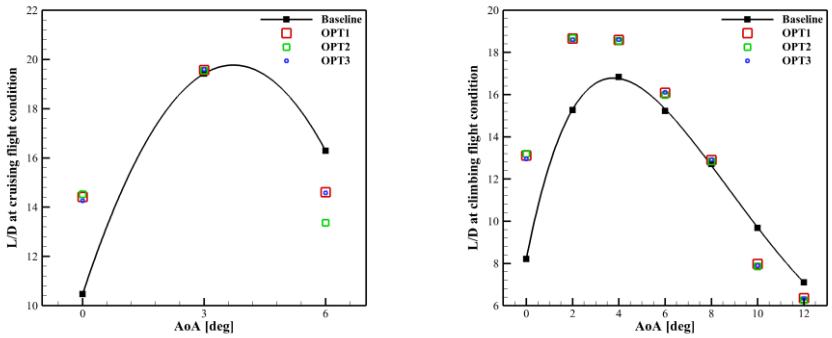

Figure 32 L/D comparison at cruising(left) and climbing(right) flight condition

Figure 32(right). They have higher L/D until AoA increases to 8˚ and become lower at AoA 10˚, 12˚ than the baseline. Because these 4 configurations have pitchbreak onset angle in the range 7˚~8˚, it can be understood that OTPS have higher L/D than the baseline in the region before the pitchbreak. The objective function(obj2) was to increase the maximum available lift in climbing flight condition, but it is encouraging that the L/D also increases as well as the maximum available lift. Also, Figure 33 shows how static stability margin changes as AoA increases. It is interesting that OPTs have lower AoA of pitchbreak onset though OPT1 and OPT3 have higher maximum available lift than the baseline. Resultant surface C_P contour of the OPTs are compared with the baseline in Figure 34 and 35. By the comparison with the baseline, it can be inferred that moderate planform modification can improve aerodynamic performance without drastic change of the flow characteristics.

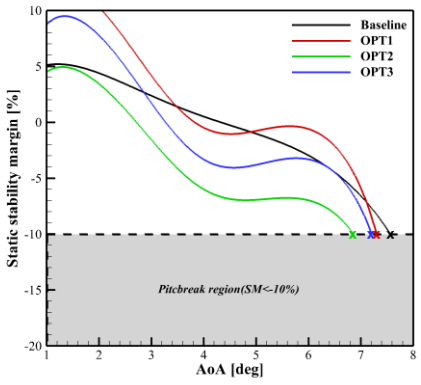

Figure 33 Comparison of static stability margin behavior

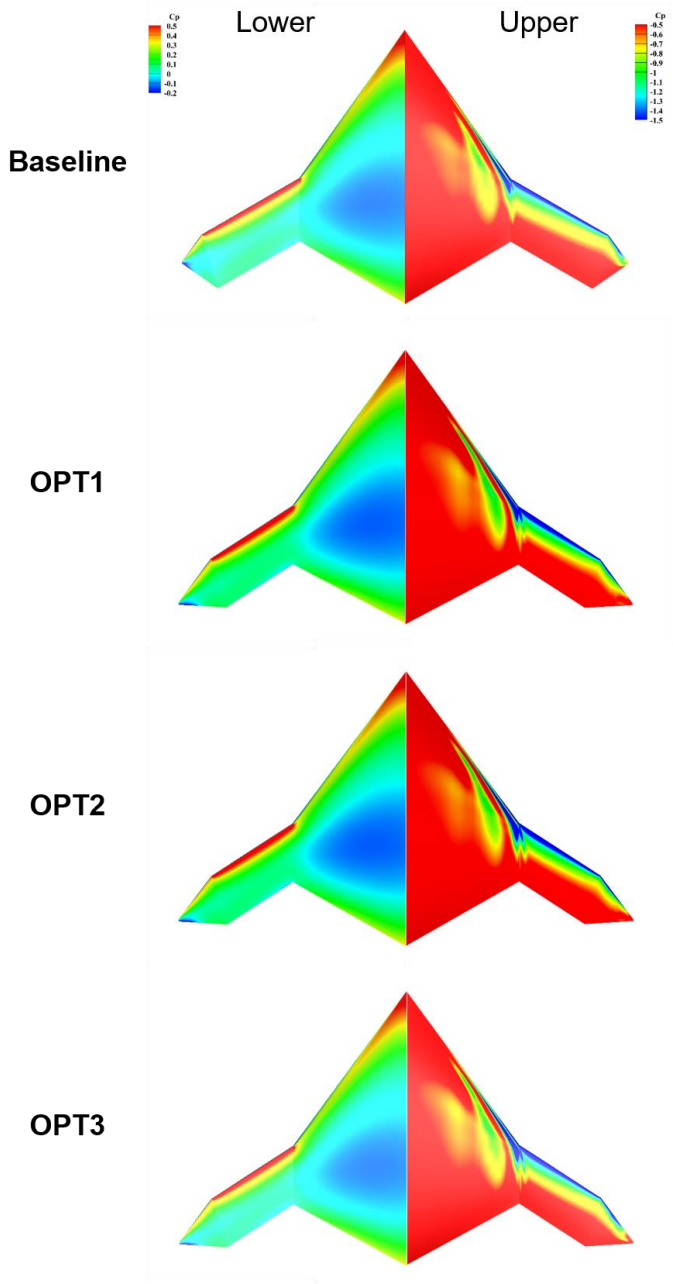

Figure 34 Surface C_P contour comparison of the lower and upper surface (@ climbing AoA 8°)

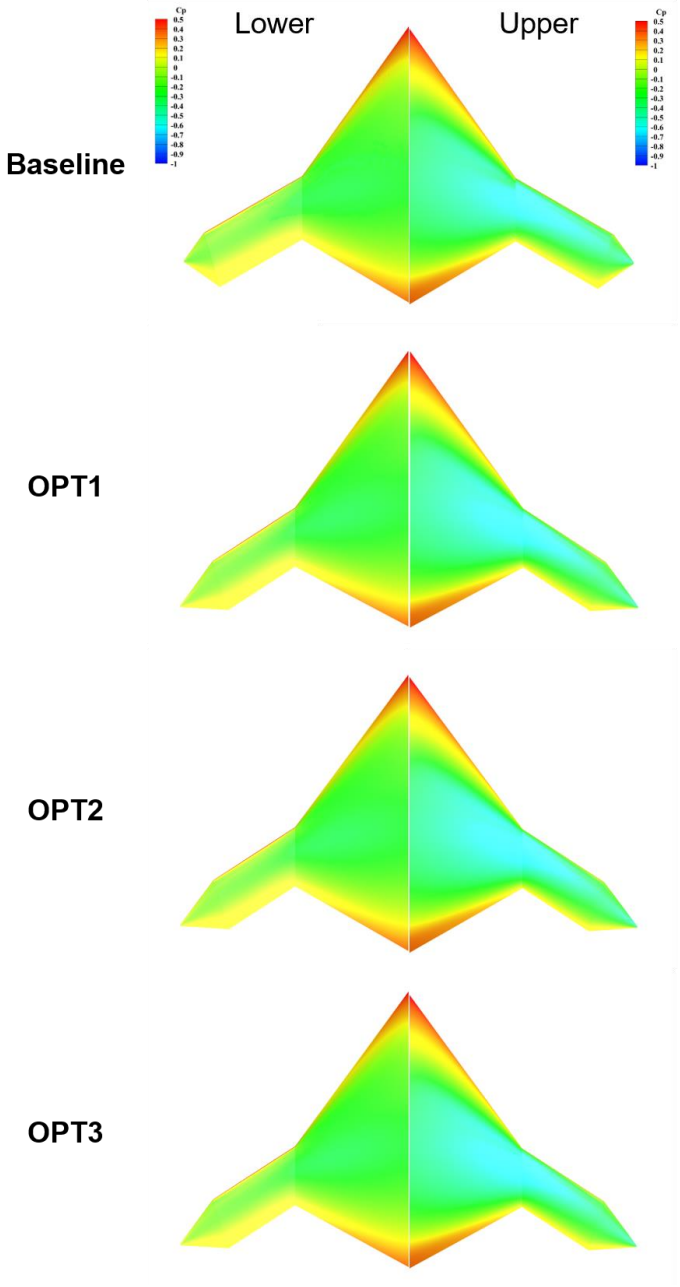

Figure 35 Surface C_P contour comparison of the lower and upper surface (@ cruising AoA 0˚)

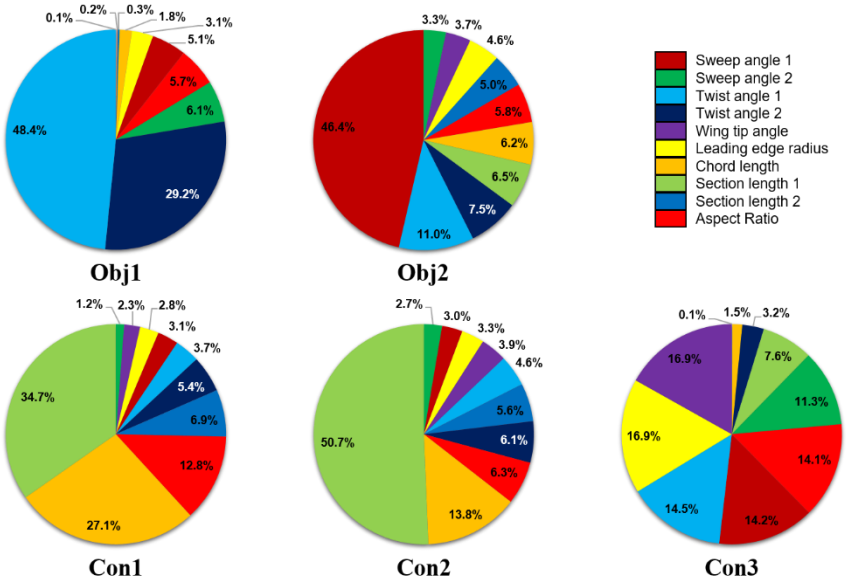

Figure 36 Results of ANOVA

The reason for the better performance of OPTs compared to the baseline can be quantitatively understood by sensitivity analysis. By Analysis of Variance(ANOVA), one can represent correlation between design variables and outputs[63]. Figure 36 shows the results of ANOVA between 10 design variables and 5 outputs. For the objective 1, twist angles take up almost 80% which indicates that cruising L/D can be improved by modifying twist angles in the planform design process of UCAV. Figure 37 shows how objective 1 varies with respect to the combination of two twist angles. It shows that cruising L/D can increases in certain region of twist angles and actually, combinations of OPTs' twist angles are within that region. Note that the objective 1 is low where both

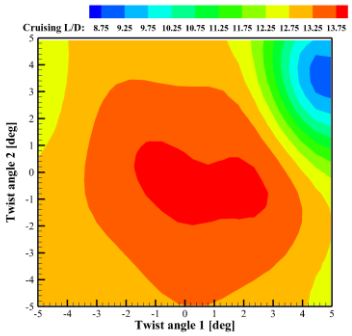

Figure 37 Correlation between obj1 and two twist angles

angles are large. Meanwhile, sweep angle 1 is the most significant factor for the objective 2. Increasing sweep angle 1 can cause the wing to form at the back, generating lift at the rear part of the planform. This effect will make the configuration stable due to the movement of the center of gravity and can be confirmed by Figure 38. In that sense, OPT2 has the smallest sweep angle 1, which is the main difference with other optimums, so that its objective 2 is the smallest(even worse than the baseline) among OPTs. Large sweep angle 1 can improve objective 2 by making UCAV stable, but its correlation with the constraint 3 prevents this to be happened as shown in Figure 39. From this, it can be inferred why OPT2 has the best performance in terms of the constraint. At the same time, two twist angles also have large influence on the objective 2 as well as objective 1. Because objective 2 is related to the lift, it can be higher as both angles increase as shown in Figure 40. However, these angles cannot be rise limitlessly due to the objective 1. It

was mentioned that large value of both angles can reduce the cruising L/D, objective 1. It was predictable that for the objective 2 which is about stability and lift, sweep angle 1 and twist angles have dominant effect, and this prediction is confirmed by sensitivity analysis.

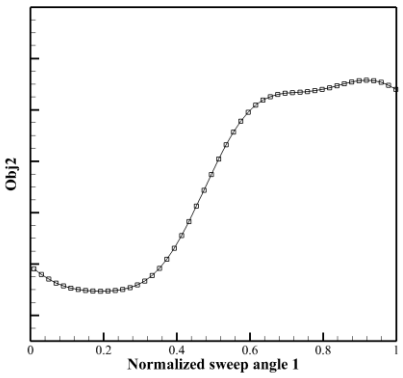

Figure 38 Sensitivity analysis between obj2 and sweep angle 1

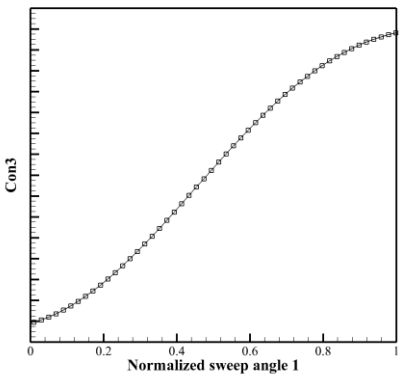

Figure 39 Sensitivity analysis between con3 and sweep angle 1

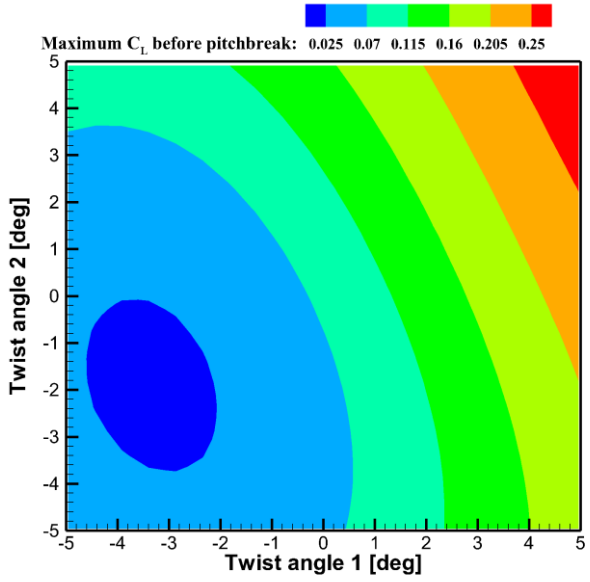

Figure 40 Correlation between obj2 and two twist angles

In summary, 3 planforms selected from the pareto set are calculated by high fidelity analysis. All of selected points satisfy the constraints. For the objectives, their performances improve with respect to the baseline except OPT2. OPT2 is estimated to have superior cruising L/D than others but it is due to the failure of the prediction of drag polar trend. Then these results from calculations are considered together with the sensitivity analysis results, and it is concluded that moderate modification of the planform can improve the L/D at cruising and longitudinal stability at climbing flight condition without radical alteration of the flow and LO characteristics from the results of OPT1 and OPT3.

IV. Conclusions

This research is about the optimization of the UCAV planform considering aerodynamic and Low-Observability characteristics. These characteristics are examined simultaneously as a multi-disciplinary design due to the trade-off relationship between them. For the optimization, L/D at cruising and stability during the climbing flight are considered as the multi-objective problem while preserving or improving the LO performance. Aerodynamic analysis is conducted by the RANS solver to capture the vortex flow accurately unlike Euler solver despite its large computational time. For the LO characteristics, RCS is computed by the SBR solver. Due to the multi-disciplinary, multi-point and high fidelity analysis, problem of the computational cost rises and it is reduced by the two-level VFM for CFD and RCS analysis. Surrogate based optimization based on the hierarchical kriging is conducted and after repetitive GA and adaptive sampling, final pareto set is obtained. 3 optimums are selected from the pareto set and calculated by the high fidelity analysis. As a result, their objectives improve compared to the baseline except OPT2. Objectives of the OPT1 improve 2.76%, 3.13% each and for the OPT3, 3.21% and 1.85%. For the OPT2, L/D at cruising improves drastically by 8.04% but it is found that this radical improvement is due to the failure of

the model which predicts the drag polar at the cruising flight condition. Meanwhile, all of these optimum points satisfy average RCS reduction which is considered as a constraint in the optimization process. Then, by the sensitivity analysis using ANOVA, correlation between used design variables and two objectives are investigated. Finally, it is concluded that the improvements of the L/D at cruising and longitudinal stability at climbing flight condition without radical alteration of the flow and LO characteristics of the UCAV are feasible by moderate modification of the planform variables. Future work will handle the more realistic planform optimization based on the certain mission profile with the accurate trim analysis at the cruising flight condition so that the precise correlation between L/D at cruising and stability at climbing flight can be analyzed.

REFERENCES

[1] Woolvin, J., "A Conceptual Design Study of the 1303 UCAV Configuration," In 24th Applied Aerodynamics Conference, 2006.

[2] Kuntawala, B., "Aerodynamic Shape Optimization of a Blended-Wing-Body Aircraft Configuration," M.S. Dissertation, Dept. of Aerospace Engineering, University of Toronto, Toronto, Canada, 2011.

[3] Siouris, S., and Qin, N., "Study of the effects of wing sweep on the aerodynamic performance of a blended wing body aircraft," In Proceedings of the Institution of Mechanical Engineers Part G Journal of Aerospace Engineering, 2007.

[4] Bolsunovsky, A. L., et al., "Flying wing-problems and decision," 2001.

[5] Stenfelt, G., and Ringertz, U., "Lateral Stability and Control of a Tailless Aircraft Configuration," Journal of Aircraft, 2009. 46(6): p. 2161-2163.

[6] Stadmore, H. A., "Radar Cross Section Fundamentals for the Aircraft Designer," In AIAA AIRCRAFT SYSTEMS AND TECHNOLOGY MEETING, 1979.

[7] Schütte, A., and Huber, K. C., "Stability and Control Investigations of Generic 53 Degree Swept Wing with Control Surfaces," Journal of Aircraft, 2018. 55(2): p. 502-533.

[8] Shim, Hojoon, and Park, Seungo, "Passive control of pitch-break of a BWB UCAV model using vortex generator," Journal of Mechanical Science and Technology, 2015. 29(3): p. 1103-1109.

[9] McParlin, S. C., et al., "Low speed wind-tunnel tests on the 1303 ucav concept," In 24th Applied Aerodynamics Conference, 2006.

[10] Nangia, R. K., and Palmer, M. E., "A COMPARATIVE STUDY OF FOUR UCAV WING LAYOUTS – HIGH SPEED AERO PERFORMANCE & STABILITY," In 25TH INTERNATIONAL CONGRESS OF THE AERONAUTICAL SCIENCES, 2006.

[11] Taha, H. E., and Hajj, M. R., "Effects of the Stealth Requirements on the Aerodynamic Performance of the X-47B," In 54th AIAA/ASME/ASCE/AHS

/ASC Structures, Structural Dynamics, and Materials Conference, 2013.

[12] Hitzel, S. M., "Aerodynamics and Radar Signature: A combination of Theoretical Methods," Journal of Aircraft, 1988. 25(5): p. 399-404.

[13] Schütte, A., et al., "Flow Physics Analyses of a Generic Unmanned Combat Aerial Vehicle Configuration," Journal of Aircraft, 2012. 49(6): p. 1638-1651.

[14] Nangia, R. K., et al., "UCAV Wing Design, Assessment and Comparisons," In 2018 Applied Aerodynamics Conference, 2018.

[15] Zenkner, S., and Becker, R., "Preliminary Engine Design for the MULDICON Configuration," In 2018 Applied Aerodynamics Conference, 2018.

[16] Aref, P., et al., "Computational Design of S-Duct Intakes for the NATO AVT-251 Multi-Disciplinary Configuration," In 2018 Applied Aerodynamics Conference, 2018.

[17] Schütte, A., et al., "Aerodynamic shaping design and vortical flow design aspects of a 53deg swept flying wing configuration," In 2018 Applied Aerodynamics Conference, 2018.

[18] Lee, Seonguk, and Kim, Chongam, "Design Optimization of Vortex Generator Array to Delay Pitch-up on Tailless Aircraft," In Tenth International Conference on Computational Fluid Dynamics, 2018.

[19] Atkinson, M., and Ferguson, F., "A Computational Fluid Dynamics Investigation of the 1303 UCAV Configuration with Deployable Rao Vortex Flaps," In 44th AIAA Aerospace Sciences Meeting and Exhibit, 2006.

[20] Jeon, Kwonsu, et al., "Multidisciplinary UCAV System Design and Optimization Using Repetitive Response Surface Enhancement Technique," In 3rd AIAA Multidisciplinary Design Optimization Specialist Conference, 2007.

[21] Tyan, M., et al., "A Tailless UAV Multidisciplinary Design Optimization Using Global Variable Fidelity Modeling," Int'l J. of Aeronautical & Space, 2017. 18(4): p. 662-674.

[22] Pan, Y., et al., "Application of Multidisciplinary Design Optimization on Advanced Configuration Aircraft," J. Aerosp. Technol. Manag., 2017. 9(1): p. 63-70.

[23] Tianyuan, H., Xiongqing, Y., "Aerodynamic/Stealthy/Structural Multidisciplinary Design Optimization of Unmanned Combat Air Vehicle," Chinese Journal of

Aeronautics, 2009. 22: p. 380-386.

[24] Jo, Yeongmin, et al., "Variable-Fidelity Design Method Using Gradient-Enhanced Kriging Surrogate Model with Regression," In 14th AIAA Aviation Technology, Integration, and Operations Conference, 2014.

[25] Sepulveda, E., et al., "Multidisciplinary analysis of subsonic stealth unmanned combat aerial vehicles," CEAS Aeronautical Journal, 2019. 10: p. 431-442.

[26] Lee, D.S., et al., "Robust evolutionary algorithms for UAV/UCAV aerodynamic and RCS design optimization," Computers & Fluids, 2008. 37: p. 547-564.

[27] Lee, D.S., et al., "Aerodynamic/RCS Shape Optimisation of Unmanned Aerial Vehicles using Hierarchical Asynchronous Parallel Evolutionary Algorithms," In 24th Applied Aerodynamics Conference, 2006.

[28] Zhang, F., et al., "A CFD Based Study of UCAV 1303 Model," In 23rd AIAA Applied Aerodynamics Conference, 2005.

[29] Hebbar, S. K., et al., "Experimental Study of Vortex Flow Control on Double-Delta Wings Using Fillets," Journal of Aircraft, 1996. 33(4): p. 743-751.

[30] Hebbar, S., et al., "EXPERIMENTAL INVESTIGATION OF VORTEX FLOW CONTROL USING JUNCTURE FILLETS ON A CROPPED DOUBLE-DELTA WING," In 33rd Aerospace Sciences Meeting and Exhibit, 1995.

[31] Schütte, A., "Numerical Investigations of Vortical Flow on Swept Wings with Round Leading Edges," Journal of Aircraft, 2017. 54(2): p. 572-601.

[32] Fujii, K., and Schiff, L. B., "Numerical Simulation of Vortical Flows Over a Strake-Delta Wing," AIAA JOURNAL, 1989. 27(9): p. 1153-1162.

[33] Rizzi, A., et al., "Comparison of Euler and Navier-Stokes solutions for vortex flow over a delta wing,"

[34] Park, Soohyung, and Kwon, Janghyunk, "Implementation of k–ω Turbulence Models in an Implicit Multigrid Method," AIAA JOURNAL, 2004. 42(7): p. 1348-1357.

[35] Kim, Jeewoong, et al., "Euler and Navier-Stokes Simulations of Helicopter Rotor Blade in Forward Flight Using an Overlapped Grid Solver," In 19th AIAA Computational Fluid Dynamics, 2009.

[36] Hoffmann, K. A., and Chiang, S. T., "Computational fluid dynamics," IV. 2000.

Engineering Education System.

[37] Menter, F. R., "Improved Two-Equation k–ω Turbulence Models for Aerodynamic flows," nasa tm 103975,(1992)

[38] Bardina, J. E., et al., "Turbulence Modeling Validation, Testing and Development," nasa tm 110446,(1997)

[39] Tannehill, J. C., et al., "COMPUTATIONAL FLUID MECHANICS AND HEAT TRANSFER," II, 1997. Taylor & Francis.

[40] Versteeg, H. K., and Malalasekera, W., "An Introduction to COMPUTATIONAL FLUID DYNAMICS," II,2007. Pearson Education.

[41] Pulliam, T. H., and Chaussee, D. S., "A Diagonal Form of an Implicit Approximate-Factorization Algorithm," JOURNAL OF COMPUTATIONAL PHYSICS, 1981. 39: p. 347-363.

[42] Jenn, D. C., "Radar and Laser Cross Section engineering," 1995. American Institute of Aeronautics and Astronautics, Inc.

[43] Davidson, D. B., "Computational Electromagnetics for RF and Microwave Engineering by Davidson," 2005. Cambridge University Press.

[44] Pienaar, C., et al., "RCS Validation of Asymptotic Techniques Using Measured Data of an Electrically Large Complex Model Airframe," ACES JOURNAL, 2017. 32(1): p. 60-67.

[45] Ling, H., et al., "Shooting and Bouncing Rays: Calculating the RCS of an Arbitrarily Shaped Cavity," IEEE TRANSACTIONS ON ANTENNAS AND PROPAGATION, 1989. 37(2): p. 194-205.

[46] https://www.ansys.com/products/electronics/ansys-hfss

[47] Woo, A. C., et al., "Benchmark Radar Targets for the Validation of Computational Electromagnetics Programs," IEEE ANTENNAS AND PROPAGATION MAGAZINE, 1993. 35(1): p. 84-89.

[48] Cavazzuti, M., "Optimization Methods: From Theory to Design," 2013. Springer.

[49] Krige, D. G., "A Statistical Approach to Some Basic Mine Valuation problems on the WITWATERSRAND," JOURNAL OF THE CHEMICAL METALLURGICAL & MINING SOCIETY OF SOUTH AFRICA, 1951. 52(6): p. 119-139.

[50] Han, Z. H., and Görtz, S., "Hierarchical Kriging Model for Variable-Fidelity Surrogate Modeling," AIAA JOURNAL, 2012. 50(9): p. 1885-1896.

[51] Han, Z. H., and Xu, C. Z., "Efficient Aerodynamic Shape Optimization Using Variable-Fidelity Surrogate Models and Multilevel Computational Grids," Chinese Journal of Aeronautics, 2019.

[52] Zhang, Y., et al., "Variable-fidelity expected improvement method for efficient global optimization of expensive functions," Struct Multidisc Optim 58, 1431–1451 (2018).

[53] Kim, Yoonki, et al., "Variable-Fidelity Optimization of Film-Cooling Hole Arrangements Considering Conjugate Heat Transfer," JOURNAL OF PROPULSION AND POWER, 2018. 34(5): p. 1140-1151.

[54] Kim, Yoonki, et al., "High-to-Low Initial Sample Ratio of Hierarchical Kriging for Film Hole Array Optimization," JOURNAL OF PROPULSION AND POWER, 2018. 34(1): p. 108-115.

[55] Jeong, Shinkyu, et al., "Efficient Optimization Design Method Using Kriging Model," Journal of Aircraft, 2005. 42(2): p. 413-420.

[56] Fonseca, C. M., and Fleming, P. J., "Genetic Algorithms for Multiobjective Optimization: Formulation, Discussion and Generalization,"

[57] Tamaki, H., et al., "Multi-Objective Optimization by Genetic Algorithms: A Review," in Proc. 1996 IEEE Int. Conf. Evolutionary Computation, pp. 517–522.

[58] Vinh, H., et al., "Airfoil Shaping for Reduced Radar Cross Section," Journal of Aircraft, 1994. 31(4): p. 787-793.

[59] Whittenbury, J. R., "Configuration Design Development of the Navy UCAS-D X-47B," AIAA Centennial of Naval Aviation Forum "100 Years of Achievement and Progress", 2011.

[60] Zikidis, K., et al., "Low Observable Principles, Stealth Aircraft and Anti-Stealth Technologies," Journal of Computations & Modelling, 2014. 4(1): p. 129-165.

[61] Brown, A. C., "Fundamentals of Low Radar Cross-Sectional Aircraft Design," Journal of Aircraft, 1993. 30(3): p. 289-291.

[62] Raymer, D. P., "Aircraft Design: A Conceptual Approach," II,1992. American Institute of Aeronautics and Astronautics, Inc.

[63] Anderson, M. J., “A new method for non-parametric multivariate analysis of variance,” Austral Ecology, 2001. 26: p.32-46.

초록

무인전투기는 무기를 싣고 적진으로 침투하는 임무 형상에 따라 장거리 및 장기 체공 왕복 비행이 가능해야 하며 이와 동시에 비행 안정성 및 적군의 레이더에 탐지되지 않는 생존성이 보장되어야 한다. 이에 따라 무인전투기 형상 설계 단계부터 공력 뿐만 아니라 다양한 성능을 동시에 고려한 해석이 필요하다. 특히 공력에 있어 앞전에서 발생하는 와류의 영향으로 인해 높은 정확도의 해석자를 필요로 한다. 하지만 기존 연구들은 형상 설계 단계에서 공력 특성만을 고려하거나 다른 특성들을 고려하여도 낮은 신뢰도의 유동 해석자를 사용한 점에서 분명한 한계를 지닌다.

따라서 본 연구는 RANS 솔버와 레이더 단면적 분석을 통한 무인전투기 플랜폼 최적화를 수행하였다. 장거리 및 장기 체공 성능과 관련되어 공력 성능 척도로 흔히 사용되는 순항 비행시의 양항비와 상승 비행 시 종방향 안정성을 잃게 되는 pitchbreak 현상이 발생하기 이전의 받음각 영역에서 발생시킬 수 있는 최대 양력을 증가시키도록 두 목적 함수를 설정하였고, 저피탐성을 고려하기 위하여 레이더 단면적을 제약조건으로 설정하였다. 이에 따라 다지점 및 다학제간 설계로 인한 과도한 계산 비용을 줄이기 위하여 다중정확도 모델링 기법으로 계층적 크리깅 대리 모델이 사용되었다. 생성된 대리 모델을 기반으로 다목적

유전자 알고리즘을 통하여 Pareto set 을 도출하였으며, 그 중 3 개의 형상을 선정하여 고정확도 해석을 진행하였다. 그 결과 기존 형상에 비하여 두 목적 함수의 성능이 향상되었으며, 민감도 분석을 통하여 설계 변수가 변화함에 따라 그들의 거동이 어떻게 변하는지 분석하였다. 본 연구는 UCAV 플랜폼의 저피탐성을 보장하면서 순항 비행시의 성능과 상승 비행시 종방향 안정성을 향상시켰다는 점에서 의의가 있다.

주요어 : 무인전투기, 공력 성능, 저피탐성, 다중정확도 모델링, 계층적 크리깅, 다목적 최적 설계

학 번 : 2018-29313